

RESEARCH PAPER



Deep learning-based detection of bacterial swarm motion using a single image

Yuzhu Li^{a,b,c,*}, Hao Li^{d*}, Weijie Chen^{d*}, Keelan O'Riordan^{a,e}, Neha Mani^f, Yuxuan Qi^{a,g}, Tairan Liu^{a,b,c}, Sridhar Mani^d, and Aydogan Ozcan^{ib,a,b,c,h}

^aElectrical and Computer Engineering Department, University of California, Los Angeles, CA, USA; ^bBioengineering Department, University of California, Los Angeles, USA; ^cCalifornia NanoSystems Institute (CNSI), University of California, Los Angeles, CA, USA; ^dDepartment of Medicine, Genetics and Molecular Pharmacology, Albert Einstein College of Medicine, Bronx, NY, USA; ^eDepartment of Physics and Astronomy, University of California, Los Angeles, CA, USA; ^fDepartment of Biochemistry and Molecular Biophysics, Columbia University, New York, NY, USA; ^gDepartment of Computer Science, University of California, Los Angeles, CA, USA; ^hDepartment of Surgery, University of California, Los Angeles, CA, USA

ABSTRACT

Motility is a fundamental characteristic of bacteria. Distinguishing between swarming and swimming, the two principal forms of bacterial movement, holds significant conceptual and clinical relevance. Conventionally, the detection of bacterial swarming involves inoculating samples on an agar surface and observing colony expansion, which is qualitative, time-intensive, and requires additional testing to rule out other motility forms. A recent methodology that differentiates swarming and swimming motility in bacteria using circular confinement offers a rapid approach to detecting swarming. However, it still heavily depends on the observer's expertise, making the process labor-intensive, costly, slow, and susceptible to inevitable human bias. To address these limitations, we developed a deep learning-based swarming classifier that rapidly and autonomously predicts swarming probability using a single blurry image. Compared with traditional video-based, manually processed approaches, our method is particularly suited for high-throughput environments and provides objective, quantitative assessments of swarming probability. The swarming classifier demonstrated in our work was trained on *Enterobacter* sp. SM3 and showed good performance when blindly tested on new swarming (positive) and swimming (negative) test images of SM3, achieving a sensitivity of 97.44% and a specificity of 100%. Furthermore, this classifier demonstrated robust external generalization capabilities when applied to unseen bacterial species, such as *Serratia marcescens* DB10 and *Citrobacter koseri* H6. This competitive performance indicates the potential to adapt our approach for diagnostic applications through portable devices, which would facilitate rapid, objective, on-site screening for bacterial swarming motility, potentially enhancing the early detection and treatment assessment of various diseases, including inflammatory bowel diseases (IBD) and urinary tract infections (UTI).

ARTICLE HISTORY

Received 14 January 2025
Revised 27 March 2025
Accepted 7 May 2025





KEYWORDS

Bacterial motility; deep learning; swarming; inflammatory bowel disease; in vitro diagnosis; microbiome test


Introduction

Motility is an intrinsic characteristic of bacteria; despite the energy expenditure, it provides high returns by enabling bacteria to acquire nutrients actively and evade harmful environments.¹ Swimming/planktonic and swarming are the two primary forms of bacterial movement mediated by flagella. Swimming involves individual bacteria propelling themselves in a single direction using flagella in liquid environments. Swarming, however, entails rapid coordinated movement of bacterial groups in

the same direction on semi-solid surfaces, facilitated by flagella and surfactants.² These two concepts, swarming and swimming, both mediated by flagella, are sometimes conflated; for example, densely populated swimming bacteria are often referred to as “a swarm of bacteria.” However, most microbiologists recognize that swarming and swimming represent fundamentally different types of motilities. Understanding their distinctions holds significant research and clinical value, because swarming bacteria can exhibit unique properties that are absent in bacteria lacking swarming capabilities. Swarming

CONTACT Aydogan Ozcan  ozcan@ucla.edu  Electrical and Computer Engineering Department, University of California, Los Angeles, CA, 90095, USA; Sridhar Mani  sridhar.mani@einsteinmed.edu  Department of Medicine, Genetics and Molecular Pharmacology, Albert Einstein College of Medicine, Bronx, NY, 10461, USA

*Equal contributing authors.

 Supplemental data for this article can be accessed online at <https://doi.org/10.1080/19490976.2025.2505115>

© 2025 The Author(s). Published with license by Taylor & Francis Group, LLC.

This is an Open Access article distributed under the terms of the Creative Commons Attribution-NonCommercial License (<http://creativecommons.org/licenses/by-nc/4.0/>), which permits unrestricted non-commercial use, distribution, and reproduction in any medium, provided the original work is properly cited. The terms on which this article has been published allow the posting of the Accepted Manuscript in a repository by the author(s) or with their consent.

bacteria can move effectively on semi-solid surfaces, and they exhibit distinctive properties when infecting hosts or demonstrating therapeutic effects, compared to bacteria that possess only swimming abilities without swarming capabilities. For example, in patients with catheter and non-catheter-associated urinary tract infections (UTI), 80% of the pathogenic clinical isolates are *uropathogenic E. coli* (UPEC).³ The primary determinant of UPEC virulence in UTI is swarm (biofilm) formation; however, in these studies, swimming cannot be excluded as a potential pathogenic factor.^{4,5} In mice, UPEC moves up from the bladder to infect the kidney; however, swarm-deficient UPEC is unable to infect the kidney.⁶ Another example is *Proteus sp.* (*P. mirabilis*), a swarming bacterium whose urinary tract virulence is notably associated with swarming behavior.^{7–10} Contrasting with the generally harmful effects typically related to swarming bacteria, recent studies suggest that the enrichment of swarming bacteria under conditions of intestinal stress may confer beneficial effects. Specifically, swarming bacteria have been shown to promote intestinal mucosal repair and alleviate inflammation, thus demonstrating therapeutic effects for inflammatory bowel diseases (IBD).¹¹

Consequently, swarming bacteria may serve as effective biomarkers for detecting several diseases. In the case of IBD, for clinical samples (fecal matter or colonoscopic aspirate) there are swarming differences between those with intestinal inflammation versus those without.¹¹ It has also been reported that the swarmer isolates from mice, for example, SM1 (isolated from control mice) and SM3 (isolated from colitic mice), differ in their swarming rates but not in their swimming rates.¹¹ Given these findings, there is a pronounced need to develop efficient and cost-effective methods for detecting the presence of swarming bacteria in, e.g., urine and fecal samples, thereby facilitating the diagnosis of infections or related diseases such as IBD.¹²

For a conventional bacterial motility test, researchers inoculate the sample on a 0.5% (w/v) or 0.3% agar surface and observe the colony expansion to determine if the sample bacteria are swimming or swarming. However, this qualitative method requires at least 10 hours, and additional experiments are needed to exclude gliding or sliding

motility. To this end, prior work has successfully distinguished the motion patterns of planktonic and swarming *Enterobacter sp.* SM3 with high efficiency and certainty on the soft agar surface, which was facilitated by the use of Polydimethylsiloxane (PDMS) chips with circular wells¹³ to amplify the differences between swarming and swimming motion patterns for clearer observation.^{14,15} This prior research has investigated the visual and physical differences between SM3 swimmers and SM3 swimmers in confinements using naked-eye-based observations assisted by Vortex Order Parameters (VOP) and spatial auto-correlation functions.¹³ Specifically, in addition to direct visual checks, image sequences of each captured video were used to calculate the velocity field and then calculate the parameters and functions,¹⁶ revealing that swimmers exhibit a single-swirl motion pattern whereas their planktonic counterparts form multiple randomly distributed local swirls within the confinements. This process requires manually marking the region of interest (ROI) and smoothing the vector field, which is relatively laborious, time-consuming, and prone to errors and thus not suitable for high-volume and automated settings. Moreover, the determination of the VOP thresholds for differentiating swarming and swimming motion patterns is subjective and relies heavily on experiential judgment, making the ambiguous patterns hard to define and further complicating the interpretation of results. Thus, there is an urgent need for an automatic, objective, and quantitative image recognition method, capable of making accurate and rapid decisions on bacterial motility types.

The rapid advancement of artificial intelligence (AI) in recent years offers a promising avenue to address this problem. Deep neural networks (DNNs) stand out due to their exceptional ability to handle high-dimensional, sparse, and noisy data exhibiting nonlinear relationships.¹⁷ This capability allows DNNs to identify subtle distinctions between similar images or videos, even in varied and noisy environments. Consequently, DNNs have been widely adopted across a broad spectrum of biomedical fields, such as microorganism detection,^{18–23} disease detection,^{24–28} and cell,^{29,30} organelle³¹ and organ segmentation,³² among others.

While AI has already been utilized to analyze bacterial motility properties for species phenotyping^{33–35} and to identify various phases of swarming development,³⁶ the direct, end-to-end differentiation of motility types, such as swarming and swimming, from raw microscopic videos or images remains largely unexplored. To address this gap, here we report a novel method of determining the type of bacterial motility on a surface. Unlike traditional video-based human-intervened swarming detection methods (Figure 1(a)), this deep learning-empowered method can rapidly and automatically identify swarming events from non-swarming planktonic motion patterns using a single blurry image, as shown in Figure 1(b). The swarming DNN classifier, developed using an attention-based neural network, was trained to distinguish between swarming and planktonic motion

patterns by interpreting specific spatiotemporal features encoded in a single image through a long integration time, yielding high specificity and sensitivity for both internal generalization (SM3 bacteria) and external generalization tests involving other types of bacteria never seen before, such as *Serratia marcescens* DB10 and *Citrobacter koseri* H6. This technique offers an automated, objective, efficient, and quantitative approach for evaluating the swarming probability of a sample. This advancement has the potential to evolve into a portable system or be integrated into a smartphone-based device together with simple disposable chips, creating a convenient, rapid, and practical method for on-site screening of microbial motility in complex samples and helping the specific and sensitive detection of various bacterial diseases.

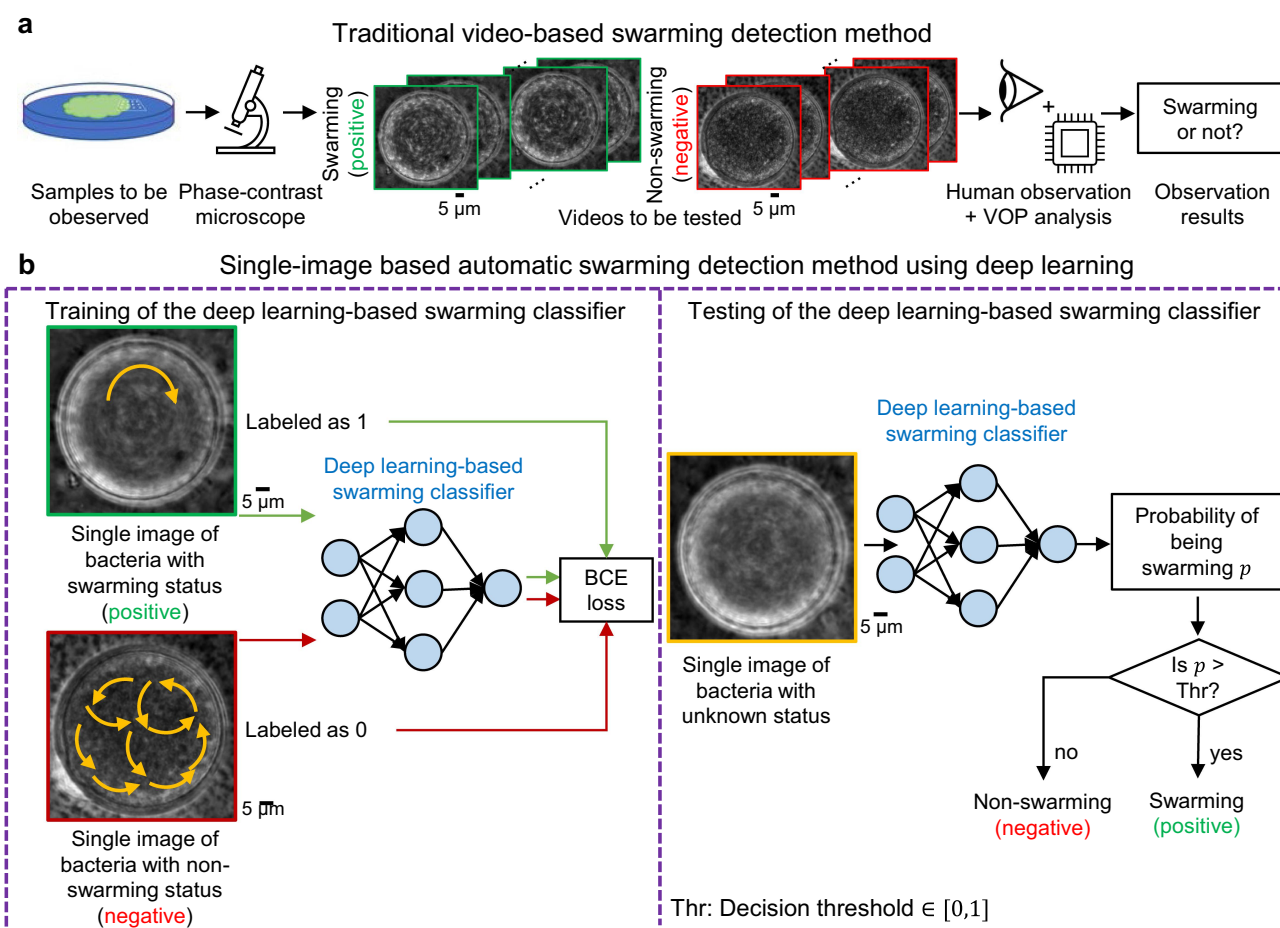


Figure 1. Deep learning-enabled bacterial motility analysis to detect swarming motion on a surface. (a) The traditional video-based swarming detection methods require human interventions and observations, which are time-consuming, laborious, and susceptible to various sources of errors. (b) The deep learning-based swarming classifier, after its training, can rapidly provide automated, and accurate predictions of bacterial motion patterns (swarming or planktonic) on unseen data using a single image with a long integration time of ~ 0.3 sec.

Results

The deep learning-enabled bacterial swarming detection neural network used in our work was built based on the DenseNet³⁷ architecture using SM3 (*Enterobacter sp.*) bacteria. Samples exhibiting swarming and planktonic states of SM3 were prepared according to a standardized protocol outlined in ref¹³ and detailed in the Methods section. These samples were then positioned under a phase-contrast microscope (Olympus CKX41, 20×) for video capture. The single image per well, serving as the input of the deep learning-based swarming classifier, was obtained by averaging 10 consecutive frames from the raw video, corresponding to a total integration time of ~ 0.34 sec per image. In this single blurry image, the time-varying bacterial movement is encoded into the spatial domain, creating distinct trajectory patterns for the swarming and swimming states of bacteria that the DNN

model can learn and differentiate. Specifically, swarming (positive) patterns are characterized by a distinct, centrally located bright ring in each long exposure image, arising from the collective and repetitive global swirling motion of SM3 swimmers. In contrast, swimming (negative) patterns resulting from the free movement of individual bacteria produce more random and featureless trajectory patterns in each long exposure image. However, a bright ring-shaped artifact located at the well edges was also observed in both the swarming and swimming bacteria samples, complicating the predictions made by the DNN model. This occurs because the bacterial movement is confined at the well edges, forcing the bacteria to move along these boundaries. To address this edge artifact and enhance the model accuracy, an attention module was integrated to the basic structure of the classifier (as shown in Figure 2). This module adaptively adjusts the radius and centroid shifts of the circular

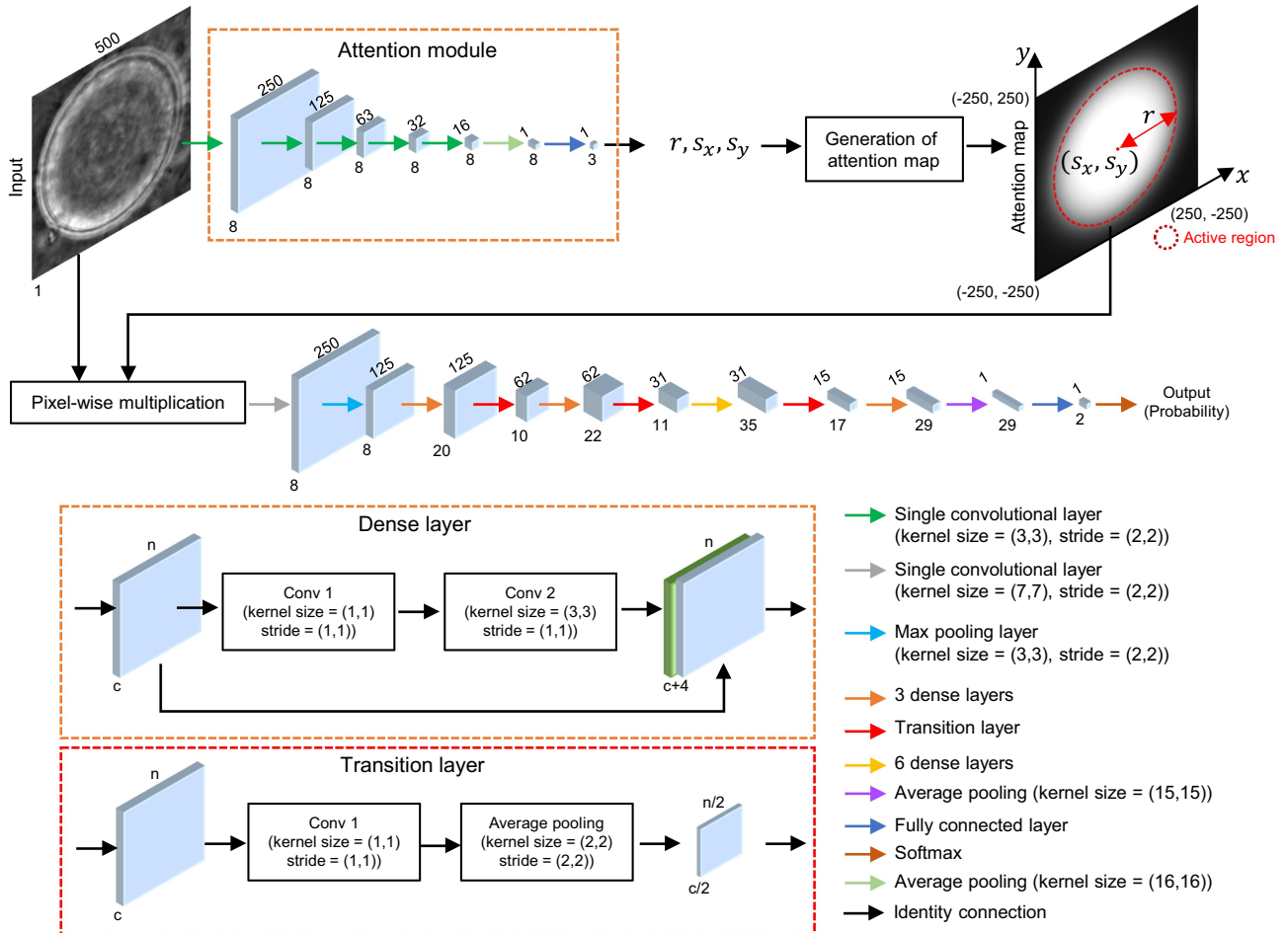


Figure 2. Network architecture of the deep learning-based swarming classifier. The DNN model was built based on the backbone of DenseNet.³⁷ The attention module is used to adaptively generate attention maps with adjustable radius and centroid shifts of the circular active region for each well.

active region for each well to mitigate the influence of peripheral bright rings.

The deep learning-based swarming classifier was trained using a dataset of 1,301 positive images from 52 wells and 2,703 negative images from 38 wells, with 90% allocated for training and the remaining 10% reserved for validation. The trained network model would predict a continuous output value ranging from 0 to 1 for each unseen test image, representing the likelihood of being swarming motility. Using a predefined decision threshold, the model blindly categorized each test well as either swarming or non-swarming based on its prediction score.

To blindly test the efficacy of our deep learning-based swarming classifier, we initially conducted tests on its internal generalization capabilities using new, unseen SM3 samples (the same type of bacteria used in training). [Figure 3\(a\)](#) showcases three representative images for each of the SM3 swarming and swimming/planktonic patterns, along with the swarming probabilities blindly predicted by our DNN model. The predicted swarming probabilities closely aligned with the ground truth labels, assigning high values to swarming patterns and low values to swimming patterns, demonstrating the model's accuracy in distinguishing between these motility patterns. Subsequently, the swarming detection DNN model underwent blind testing on a large dataset comprising 39 SM3 swarming (positive) well images from 5 independent experiments and 44 SM3 swimming/planktonic (negative) well images from 7 independent experiments, achieving a sensitivity of 97.44% and a specificity of 100%. Detailed confusion matrix results are presented in [Figure 3\(a\)](#).

Next, we extended our blind testing of the deep learning-based swarming classifier to include two new bacterial strains, DB10 (*Serratia marcescens* Lab strain) and H6 (*Citrobacter koseri*), which were not included in the training set; this constitutes an external generalization test on the trained classifier. The classification results are summarized in [Figure 3\(b\)](#). For DB10, when tested on 48 swarming (positive) well images from 5 independent experiments and 31 swimming/planktonic (negative) well images from 5 independent experiments, our DNN model achieved a sensitivity of 97.92% and a specificity of 96.77%. Similarly, for H6, the model was tested on 27 swarming (positive) well

images from 5 independent experiments and 36 swimming/planktonic (negative) well images from 5 independent experiments, achieving a sensitivity of 100% and a specificity of 97.22%. Detailed confusion matrices for the DB10 and H6 classification performance are also presented in [Figure 3\(b\)](#). The high accuracy achieved with these new bacterial types demonstrates the robust external generalization capability of the trained DNN model. This suggests that the features the network learned to differentiate between swarming and swimming patterns are not specific to a type of bacteria, which allows for successful generalization to other bacteria strains without the need for retraining or transfer learning, highlighting the model's versatility and adaptability. Three exemplar positive videos (one each for SM3, DB10, and H6) and three exemplar negative videos (one each for SM3, DB10, and H6) together with their corresponding swarming probability scores predicted by our deep learning-based swarming classifier are reported in Supplementary Videos 1 and 2, respectively.

To further evaluate the classification performance of our deep learning-based swarming classifier, we plotted the changes in sensitivity and specificity across varying decision thresholds for the SM3, DB10, and H6 strains, as shown in [Figure 4\(a,d,g\)](#) for sensitivity and [Figure 4\(b,e,h\)](#) for specificity. Additionally, Receiver Operating Characteristic (ROC) curves for each bacteria type are depicted in [Figure 4\(c,f,i\)](#), illustrating the trade-off between the true positive and the false-positive rates at different threshold settings. The Area Under the Curve (AUC) is also reported in each case, demonstrating a very good classifier performance with scores of 0.9988 for SM3, 0.9933 for DB10, and a perfect score of 1.0 for H6. These metrics underscore the swarming classifier's high accuracy and robustness, demonstrating its strong internal and external generalization performance, also highlighting its effectiveness in accurately distinguishing between swarming and planktonic motion patterns across different types of bacteria.

Discussion

To underscore the importance of differentiating bacterial swarming behavior, it is instructive to examine the pathological mechanisms of urinary

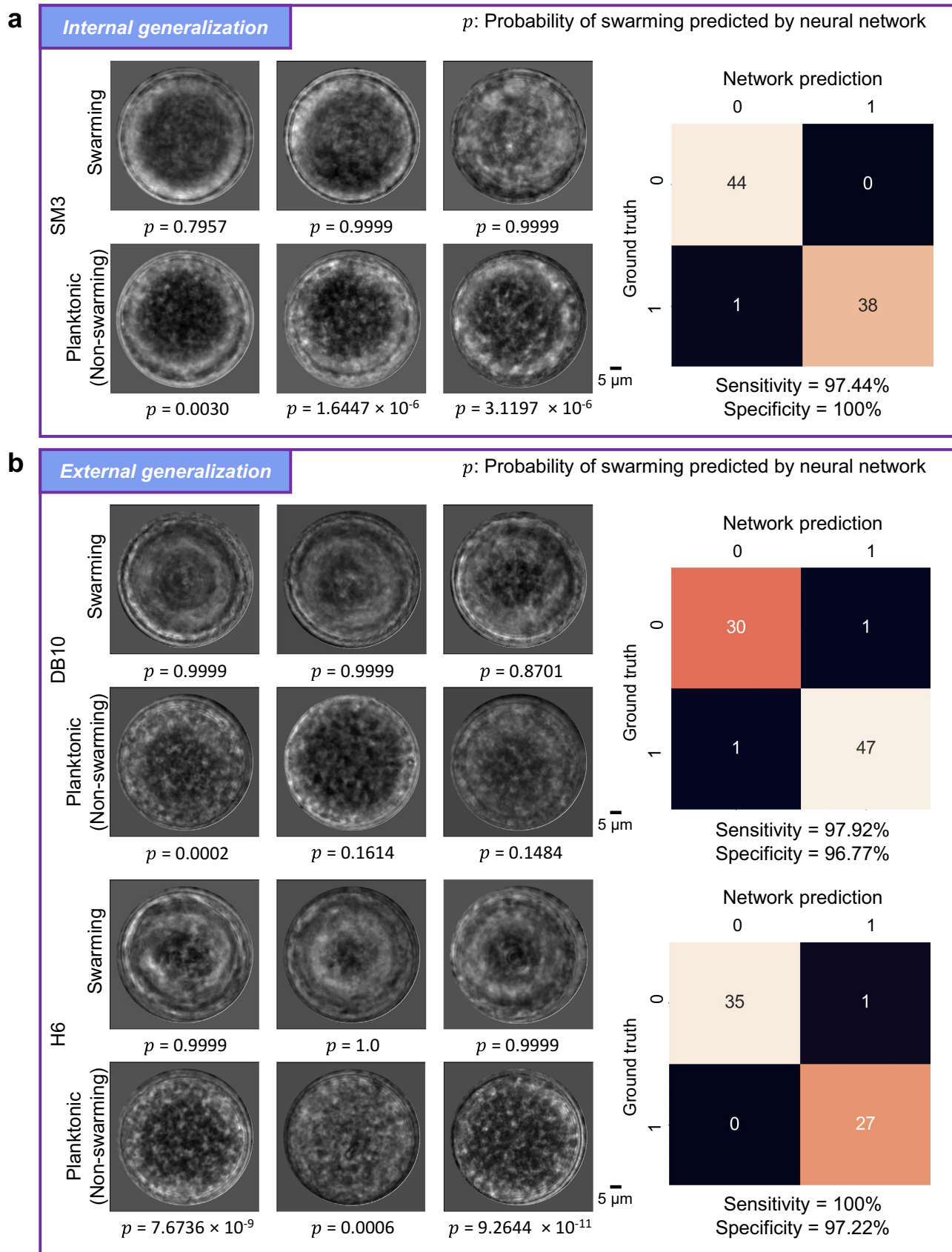


Figure 3. Swarming detection performance of the deep learning-based classifier in blind testing across SM3, DB10, and H6 bacterial strains. (a) Three example images for each of the SM3 swarming and swimming/planktonic patterns, along with the swarming probabilities predicted by our DNN model (left). The confusion matrix tested on a dataset composed of 39 swarming (positive) well

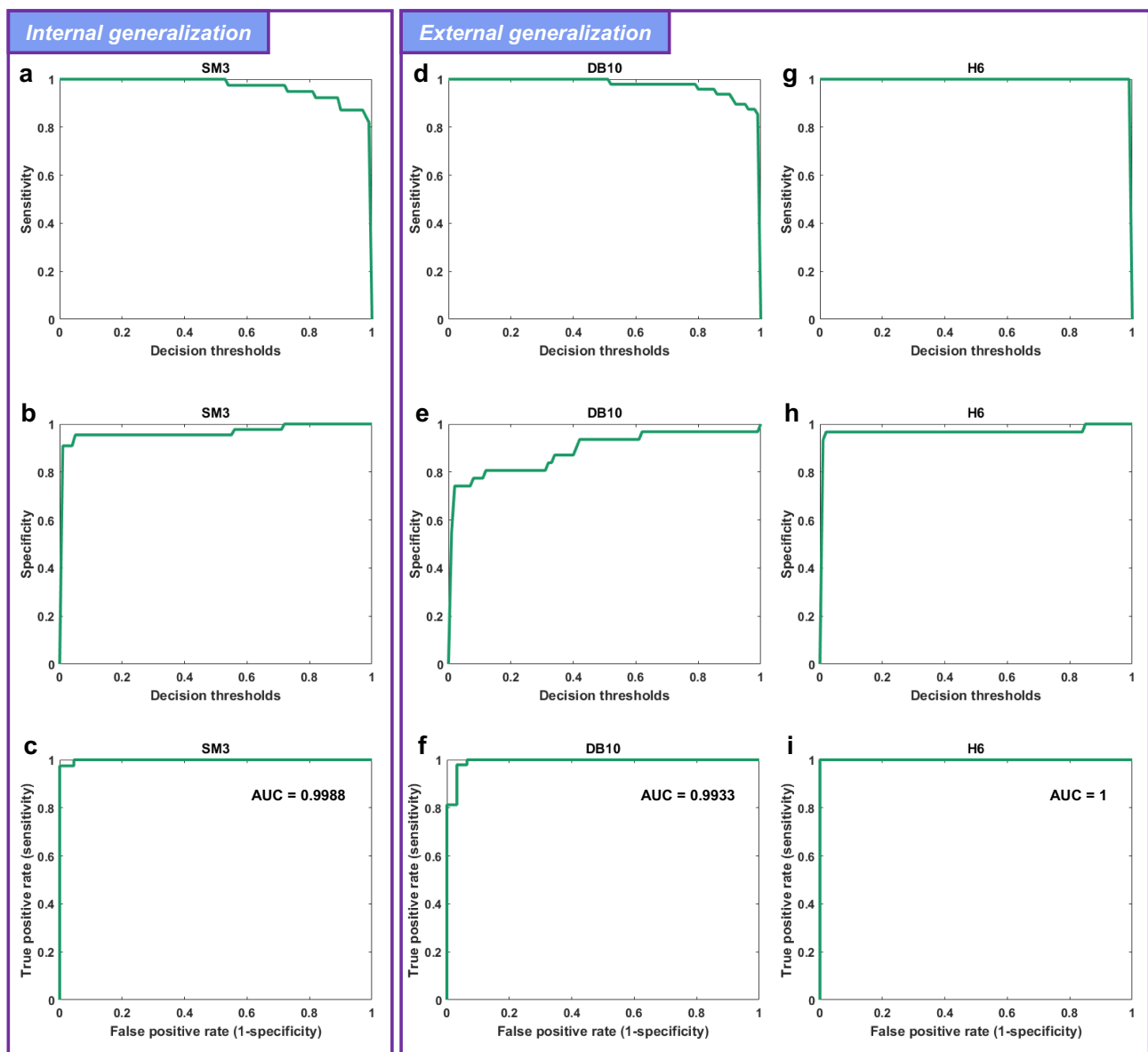


Figure 4. Sensitivity and specificity curves at varying decision thresholds, alongside the ROC curves for the deep learning-based swarming classifier, in blind testing across SM3, DB10, and H6 bacterial strains. (a) The sensitivity vs. The decision thresholds for SM3 using the same test dataset in Figure 3. (b) The specificity vs. The decision thresholds for SM3 using the same test dataset in Figure 3. (c) The ROC curve for SM3 using the same test dataset in Figure 3, with AUC = 0.9988. (d-f) same as (a-c), but for DB10, with AUC = 0.9933. (g-i) same as (a-c) and (d-f), but for H6, with AUC = 1.0.

tract and gastrointestinal infections. In addition to the unique role of swarming bacteria as pathogens in UTI, as described previously, bacterial swarming is also closely related to therapeutics for UTI. Specifically, the probiotic, non-swarming *E.coli* 83972, which was endorsed by the European

Association of Urology Guidelines in 2015, shows significant preventative (and antibiotic sparing) properties. This strain of bacteria cannot swarm or swim because of poor flagella formation; but can colonize without virulence. A recent report, showed that in individuals with *E. coli* 83972

images and 44 planktonic (negative) well images, together with the reported sensitivity and specificity are shown on the right to demonstrate the model's internal generalization ability. (b) Same as (a), but for the blind testing results of DB10 (48 positive well images and 31 negative well images) and H6 (27 positive well images and 36 negative well images), demonstrating the external generalization capability of the same DNN model.

colonization, who became symptomatic of UTI, the *E. coli* 83972 restored its flagellar machinery and became motile (without a change in other factors). This suggests that motility in UTI can be conditionally pathogenic.³⁸ Moreover, bacterial swarming colony inhibitors, typically those that affect quorum sensing, are a non-antibiotic strategy used to combat inflammation and virulence.^{39–47}

Swarming bacteria also play a vital role in gut health. In the normal gut, bacteria downregulate flagella or motility gene synthesis,⁴⁸ but patients with IBD have an increased number of bacterial swimmers present in colonoscopic aspirates and feces.^{11,49} Several pathogens like *salmonella* and *proteus* are implicated in IBD and have swarming properties. These observations directly implicate swarming in pathogenesis, rather than protection against intestinal inflammation. In contrast, our prior work suggests that commensal swarming bacteria could protect against host inflammation and provide a cue to developing personalized probiotics.¹¹ In the context of IBD, feces from patients showed a significant upregulation of flagella and the motility apparatus as compared to healthy donors.⁵⁰ This implies that early swarm flow detection in feces could be developed into diagnostic tests for IBD. More importantly, early isolation of the dominant swarming strain might provide novel probiotics for IBD, with the advantage of this approach being autologous rather than heterologous.⁴⁹ These emphasize the necessity to develop efficient and cost-effective methods for detecting swarming bacteria in urine and fecal samples, thereby allowing for rapid diagnosis of infections and associated diseases.

In this work, we developed an AI-based motility test model capable of rapidly and accurately predicting the probability of swarming within each test confinement using a single image with a long integration time of ~0.3 sec. Compared with colonoscopy or fecal microbiome metagenomic analyses, such a noninvasive and economical AI-based motility test would offer several advantages, including reduced discomfort for the patient, cost-effectiveness, rapid result delivery, and user-friendly readouts. Furthermore, apart from the initial sample collection and image capturing, the following detection process is fully automated, requiring minimal human supervision and

parameter tuning. This not only saves labor but also ensures an objective and quantitative assessment free from personal bias. Particularly valuable in high-volume settings (e.g., multiple biological samples grown in multi-well plates), our method significantly reduces reliance on human expertise and increases detection throughput compared to human-intervened observations, thereby potentially enabling efficient on-site screening for related diseases. Another important feature of the presented approach is its ability to automatically detect the motility signal earlier. Examiners do not need to wait for the colony to grow into a large size, and a small colony of ~2 cm in diameter is sufficient for the test. Additionally, our method is adaptable to various application scenarios, allowing for adjusting sensitivity or specificity preferences based on specific needs through flexible decision threshold settings. For instance, in situations where diseases or infections could cause severe consequences, detection sensitivity of our method can be increased by lowering the decision thresholds (with a compromise in specificity). Conversely, in cases where treatments are painful or resource-intensive, detection specificity can be enhanced by setting higher thresholds in our method (with a compromise in sensitivity). Notably, this decision threshold adjustment will be a one-time effort tailored to each specific application scenario, which is inherently different from the intensive parameter tuning for each individual measurement as required by traditional analysis methods. Finally, the single-image-based detection mechanism in our method does not require advanced microscopes with high frame rates. This facilitates the possibility of transferring the AI-based detection algorithm, along with disposable PDMS chips, to portable devices, even smartphones, which could potentially be used to predict real-time swarming probability.

The success of our deep learning-based swarming classifier lies in the incorporation of the attention module to mitigate edge artifacts. These bright, ring-shaped artifacts, present in both positive and negative well images, can interfere with the network's ability to learn useful features, thereby degrading the classifier's performance. To further demonstrate the importance of the attention module used in our workflow, we conducted an ablation

study by training another deep learning-based classifier using identical network architectures and training settings, except for the removal of the attention module. The results, presented in Supplementary Figure S1, clearly show the superiority of the model with the attention module, which shows higher sensitivity and specificity for both internal and external generalization tests compared to the model without the attention module. The integration of the attention module not only preserves high model accuracy but also prevents potential data loss that could arise from using a fixed radius for the circular active regions across all input images. To explicitly illustrate the function of the attention map, we expanded the single-image neural network inputs (one positive example and one negative example) into their original sequences of 10 consecutive raw video frames, overlaying each frame with the complementary region of the circular attention map (shaded in yellow), as shown in Supplementary Figure S2. Individual bacterial movements are distinctly visible within the central region defined by the attention map, whereas undesirable bright-ring artifacts appearing at the outer edges are effectively excluded. This visualization highlights a clear spatial correlation between bacterial motility regions and the boundaries delineated by the attention maps, illustrating these maps' capability to selectively preserve critical motion-related information within the active region while suppressing peripheral artifacts.

Moreover, the rationale for utilizing circular attention maps, as opposed to other shapes, is motivated by the circular geometry of the confinement wells and the inherent tendency of collective bacterial motility to form circular or vortex-like trajectories due to hydrodynamic interactions.⁵¹ Consequently, a circular attention map can more effectively capture these intrinsic motility patterns, thus enhancing our classification accuracy. To further validate this design choice, we trained an additional neural network using rectangular attention maps, with details provided in the Methods section, while keeping the network structure and training hyperparameters consistent across the experiments. The comparative analysis, presented in Supplementary Figures S3(a – b), reveals a noticeable reduction in the classification

performance with rectangular attention maps, particularly affecting the detection sensitivity for strain DB10. A representative comparison of circular and rectangular attention maps applied to the same swarming well is also illustrated in Supplementary Figure S3(c).

Another important factor impacting the network performance is the integration time used to generate single-image network inputs, which can mimic various exposure durations in practical imaging scenarios. Supplementary Figure S4(a) shows integrated images from both a positive and a negative well, created by averaging/integrating different numbers of consecutive frames (1, 5, 10, 15, and 20) from raw video data. This analysis suggests an optimal integration time that achieves maximum contrast between the swarming (positive) and planktonic (negative) states. When the integration time is too short, such as a single frame, bacterial trajectories do not accumulate adequately, leading to poor differentiation between the two states; notably, the positive wells do not obviously display the characteristic “bright-ring” pattern indicative of collective bacterial swarming movement. Conversely, excessively long integration time also diminishes the distinction between positive and negative wells, as the random movements of planktonic bacteria will eventually cover the entire imaging area, making negative wells appear like positive ones. This observation was quantitatively validated through an image contrast analysis detailed in Supplementary Figure S4(b – e). A ROI, shaded in yellow in Supplementary Figure S4(b), primarily encompasses the “bright-ring” like features that differentiate swarming from swimming motilities. The average intensity within this ROI was measured for both positive and negative wells, as shown in Supplementary Figure S4(c – d). The contrast was calculated as the scaled intensity difference between the positive and negative well groups, with the highest contrast achieved with an integration of 10 frames, as demonstrated in Supplementary Figure S4(e). This optimal choice was further substantiated by assessing the classification accuracy (Supplementary Figure S4(f)) of neural networks trained with varying numbers of integration frames, where integrating 10 consecutive frames (equivalent to an integration time of 0.34 s) achieved the highest accuracy across the test

dataset comprising three bacterial strains (SM3, DB10, and H6). Strain-specific analysis showed that while a 10-frame integration was most effective for SM3 and DB10, a shorter 5-frame integration was optimal for H6. This can be attributed to several factors, such as differences in bacterial movement speed, density per well, and the unique motility characteristics of each strain. Given these comprehensive qualitative and quantitative insights, a 10-frame integration (0.34 s) was thereby established as the standard condition used in this study. For further details on the image contrast analysis and neural network training methods under varying frame integration settings, please refer to the Methods section.

Future explorations. Although we achieved very high classification accuracy on the blind testing dataset, the neural network still produced two false negatives (one SM3 well and one DB10 well) and two false positives (one DB10 well and one H6 well), as shown in Supplementary Figure S5(a). In these cases, the misclassified images typically exhibit ambiguous or borderline features and tend to lie near the decision boundary, as evidenced by our t-distributed Stochastic Neighbor Embedding (t-SNE)⁵² feature projection analysis reported in Supplementary Figure S5(b), with features extracted using a pre-trained Visual Geometry Group (VGG-16) model;⁵³ also see the Methods section. Such errors could potentially be mitigated by adopting more advanced network architectures, augmenting the training data with additional examples, and refining the attention mechanism.

Strain-specific motility patterns can be used to distinguish surface adhesion of virulent versus probiotic *E.coli*.⁵⁴ These observations may also apply to other bacterial strains where a species may have several sub-strains, some possessing host beneficial, and others host virulent properties. The deep learning-based AI motility detection method demonstrated in our work could potentially be extended to provide predictions for host beneficial or virulent properties based on motility patterns alone. To ensure the prediction accuracy, a comprehensive analysis of swarm and swim motility could be conducted on both soft and hard surfaces, encompassing multiple bacterial strains and different rheological surfaces (e.g., mucins).

A priori knowledge of the strains that are virulent versus beneficial could serve as the ground truth. After the AI model's prediction, beneficial swarming strains could then be curated for various applications such as probiotics or for drug delivery,⁵⁵ and under external convection methods.⁵⁶

Moreover, deciphering swarming type formations under confinement in *mixed* bacterial cultures could be set as future work based on the current deep-learning swarming detection method and then tested combinatorically using multiple swarming and non-swarming species mixed. However, it is important to note that for detecting the dominant swarmer grown out from fecal samples, the single-strain bacterial swarming identification presented in our study is already valuable because there is always one swarmer strain showing up on the edge of the sample colony.¹¹ Another future goal could be to test the motility detection model in environments that introduce obstacles to flow fields in confinement. For example, it could be tested using actual fecal samples that would have such obstructions (e.g., non-motile food particles). Through these future studies, it might be possible to attain AI-based prediction models for determining swarm-like patterns in complex media like feces or soil. This strategy could eventually be used to monitor host symbiosis or the emergence of a motile pathogen,⁵⁷ soil bacteria, relationships between soil conditions and plant (crop) health,⁵⁸ or even climate change via for example, effects on coral bacteria.^{59–62} The automated plug-and-play determination of the probability of swarming could be studied in the context of chemo-attractants embedded into the agar to see which environmental or xenobiotic chemicals could trigger acceleration or diminution of swarm behavior. Contextually, these chemicals could serve to either therapeutically inhibit bacterial swarming (e.g., catheter-induced urinary tract pathogens)⁵² or aid in the swarming phenotype (e.g., gut-induced inflammation).⁶³ Similar approaches have been investigated for individual species of bacteria.⁶⁴

Study limitations. In our paper, we used selected gram-negative bacterial species isolated from feces (SM3, H6) as well as a laboratory strain (DB10).

Indeed, while obligate anaerobes do not swarm,⁶³ there are some gram-positive bacteria that do (e.g., *B. subtilis*) and these types of bacteria have not been examined in detail in the current work. The strains we used have a typical moving speed of $\sim 30 \mu\text{m/s}$ and cell length of $\sim 3 \mu\text{m}$, which are representative of motile bacteria. There may exist some statistically outstanding combinations of bacterial cell length and swimming speed, altering the confined collective motion pattern, which will be covered in future studies. Moreover, the deep learning-based swarming detection models in our work were derived using smooth agar surfaces at fixed humidity and ambient temperature conditions, which could be sufficient for creating a standardized clinical test, but rheologically different surfaces or agar gel media (e.g., rough agar, mucin, different agar compositions for the swarm plates) have not been examined yet. In the future, these conditions will be thoroughly explored, and using a graded motility library of bacterial mutants (e.g., iCRISPR library⁶⁵) we can potentially adapt the model parameters for a broader context as movement can be altered in subtle ways between strains. Furthermore, within the body, different environments may be encountered, and the switch between swimming and swarming behaviors may naturally occur.

All in all, the plug-and-play automated classification of bacterial motility using a single image with a long integration time of ~ 0.3 sec is a major step forward from the state of the art. Further studies on mixed bacteria environments in real fecal samples and user-friendly refinements of the current work could potentially lead to the development of a practical application (e.g., for smartphones), capable of capturing images and processing them in real-time, offering a convenient and immediate method for analyzing bacterial motility in various settings.

Materials and methods

Sample preparation and imaging

The bacteria strains used in this study are SM3 (*Enterobacter sp.*, isolated from inflammatory mice by Mani Lab,¹¹ DB10 (*Serratia marcescens*; lab strain provided by Cornelia Bargmann at Rockefeller University) and H6 (*Citrobacter koseri*, isolated from human colonoscopy aspirates by Mani Lab.¹¹

Sample and PDMS preparation procedures were based on the protocols presented in ref.¹³ Briefly,

bacteria strains were transferred from -80°C glycerol stock to fresh LB (Lysogeny Broth: water solution with 10 g/L tryptone, 5 g/L yeast, and 5 g/L NaCl) and shaken overnight (~ 16 hours) in a 37°C incubator at 200 rpm. Then, 2 μL overnight bacterial culture was inoculated on the center of an LB agar plate (10 g/L tryptone, 5 g/L yeast, 5 g/L NaCl, and 5 g/L agar; volume = 20 mL/plate) and placed in a 37°C incubator. After the population of bacteria started swarming for 6 hours, a PDMS chip ($\sim 1 \text{ cm}^2$) was mounted upon the edge of the swarming (positive). Each well on the PDMS chip has a diameter of $74 \mu\text{m}$. Similar concentration of freshly grown bacterial culture in LB medium (10 μL) were inoculated on 0.5% LB agar plate, and the PDMS chip was mounted immediately (exhibited planktonic or negative). Once the samples were prepared, they were positioned on a phase-contrast microscope (Olympus CKX41, 20 \times) for video capture at a frame rate of 29 fps. The imaging FOV spans approximately $422 \times 353 \mu\text{m}^2$, corresponding to 2448×2048 pixels.

Image processing and training/validation dataset preparation

After the video acquisition of bacteria exhibiting swarming (positive) or planktonic (negative) status, the training/validation dataset was prepared following the image processing workflow reported in Supplementary Figure S6. This step can also be automated using the Hough Circle Transform, as demonstrated in Supplementary Figure S7, to identify and select intact circular wells for analysis. First, the centroid coordinates of the individual well/confinement were manually selected for each video. Image sequences centered on these coordinates were then spatially cropped from the entire imaging FOV using a window size of 500×500 pixels ($\sim 86 \times 86 \mu\text{m}^2$) across all time points. To obtain a single image per test well for training/validating the deep learning-based swarming classifier, every 10 consecutive frames of the cropped image sequences were averaged over the time domain, mimicking a $10\times$ longer integration time. The resulting single image was then normalized to have a zero mean and unit variance. Furthermore, to eliminate any interference from background features or noise, the intensity values of the regions outside the well were set to zero. It is important to

note that the labels for the well images in our study are derived unambiguously due to the distinct experimental protocols used to prepare the wells for swarming (positive) and planktonic (negative) states, as described in the previous section. Specifically, all the negative samples were sourced from control experiment protocols, while all the positive samples originated from experiments intended to induce swarming. This method effectively precludes the possibility of label confusion between the positive and negative wells. Additionally, each well image was meticulously inspected manually to exclude any wells that exhibited defocusing or poor contrast. In total, the dataset includes training/validation images from 52 wells across 6 swarming experiments and 38 wells from 10 planktonic experiments. By employing data augmentation over time, varying the start and end points of the 10-frame sequences used for averaging, we generated 1,301 positive and 2,703 negative images that were used for training and validation.

Network structure and training schedule

The deep learning-based swarming classifier was developed using DenseNet³⁷ as its architectural backbone, with its detailed structure illustrated in Figure 2. Before the DenseNet structure, an attention module, constructed using a standard convolutional neural network, was exploited to adaptively determine the radius r and centroid shifts (s_x and s_y) of the circular active region on the attention map. This attention map was generated by the sigmoid function defined below,

$$Attn_map_circle_{(x,y)} = \frac{1}{1+e^{-(k(r^2-(x-s_x)^2-(y-s_y)^2)))}} \quad (1)$$

where r , s_x and s_y are the parameters predicted by the attention module, and x and y are the image indices in the horizontal and vertical directions, ranging from $[-250, 250]$ pixels. k is the factor to adjust the slope of the sigmoid function, which was empirically set to 0.0001. Moreover, the r predictions were constrained in the range of $[160, 230]$ pixels, and the s_x and s_y predictions were constrained within $[-10, 10]$ pixels. Due to the continuous differentiability of the sigmoid function, generating attention maps using this

function instead of binary segmentation ensures that gradients are properly backpropagated during the training process. For the comparative neural network utilizing a rectangular attention map, the attention module outputs parameters that differ from those used to define the circular attention map. Rather than outputting the radius r and centroid shifts (s_x and s_y), the attention module specifies the height h , width w , and centroid shifts (s_x and s_y) to define the rectangular attention area. This rectangular attention map is generated using the following formula:

$$Attn_map_rectangle_{(x,y)} = \frac{1}{1+e^{-(k(x-(s_x-\frac{w}{2})))}} \cdot \frac{1}{1+e^{-(k((s_x+\frac{w}{2})-x))}} \cdot \frac{1}{1+e^{-(k(y-(s_y-\frac{h}{2})))}} \cdot \frac{1}{1+e^{-(k((s_y+\frac{h}{2})-y))}} \quad (2)$$

where h , w , s_x and s_y are the parameters predicted by the attention module for defining the position and dimension of the rectangular attention map, and x and y are the image indices in the horizontal and vertical directions, ranging from $[-250, 250]$ pixels. k was empirically set to 0.05. The h and w predictions were constrained in the range of $[320, 460]$ pixels, and the s_x and s_y predictions were constrained within $[-10, 10]$ pixels. After obtaining the attention map, it was pixel-wise multiplied with the input image. The resulting image served as the final input for the DenseNet module to mitigate edge artifacts – specifically, the peripheral bright rings observed in both the positive and negative test well images. Utilizing the attention mechanism, rather than setting a fixed value for r , s_x and s_y , allows to adapt dynamically based on the current input. This approach not only helps eliminate edge artifacts but also ensures the retention of the most valuable information in each test image and tolerates unavoidable centroid shifts during the image cropping process.

The loss function we used to train the swarming classifier network is the weighted cross-entropy loss defined as

$$l(p, g) = \sum_{k=1}^K \sum_{l=1}^2 -w_l \times g_{k,l} \times \log\left(\frac{\exp(p_{k,l})}{\exp(p_{k,1}) + \exp(p_{k,2})}\right) \quad (3)$$

where p presents the network output, which is the probability score for each class (swarming or non-

swarming) before the SoftMax layer, and g is the ground truth, which was set to 0 (negative, non-swarming) or 1 (positive, swarming) in our binary classification setting ($g_{k,1} = 1$ for positive class, $g_{k,2} = 0$ for negative class), K is the total number of training instances in one batch ($K = 32$). w_l is the weight assigned to each class to balance the uneven positive/negative sample distributions, which is defined as $w_l = 1 - d_l$, where d_l is the percentage of the samples in class l ($d_1 = 32.5\%$ for the positive class, $d_2 = 67.5\%$ for the negative class).

During the training process, we exploited techniques such as batch normalization and dropout (with a rate of 0.5). Image flipping and rotation were utilized when loading the training dataset for data augmentation. The network model was optimized using the Adam optimizer,⁶⁶ which incorporated a momentum coefficient of (0.9, 0.999). The initial learning rate was set at 10^{-3} and was reduced by a scheduler with a coefficient of 0.9 every 10 epochs. Our model was trained on an Nvidia GeForce RTX 3090 GPU with a batch size of 32. The final model used in our work was selected based on the lowest validation loss. Once the model is obtained, it only takes 0.4 seconds to predict the motility type (swarming or non-swarming) for one test well image. The fixed decision threshold during the testing phase (for generating Figure 3) was set at 0.72, which was determined from the validation dataset to maintain maximum sensitivity while achieving 100% specificity.

Contrast analysis and network performance evaluation

To investigate how the number of integration frames used for generating single-image network inputs influences the neural network performance, we performed a contrast analysis on the ROIs containing the “bright-ring” features that distinguish swarming from swimming motilities. The ROI for a certain well was defined as a ring with an inner radius of 100 pixels ($\sim 17.3 \mu\text{m}$) and an outer radius of 180 pixels ($\sim 31.1 \mu\text{m}$). We then calculated the average intensity within this ROI (I_{pos} for positive wells and I_{neg} for negative wells) using single images generated by averaging 1, 5, 10, 15, or 20 consecutive frames from the raw videos. Next, these average

intensities were computed across all 114 positive and 111 negative wells in the blind test set, yielding the final values ($\overline{I_{pos}}$ and $\overline{I_{neg}}$) for each integration setting (Supplementary Figure S4(c – d)). We subsequently quantified the signal difference between the positive and negative wells by defining the signal contrast as:

$$\text{Signal contrast} = \frac{\overline{I_{pos}} - \overline{I_{neg}}}{\overline{I_{pos}} + \overline{I_{neg}}} \quad (4)$$

The signal contrast values for each integration setting are shown in Supplementary Figure S4(e). In addition, we trained four additional swarming detection neural networks, each using single images averaged from 1, 5, 15, or 20 frames, respectively. Including our standard setting of 10-frame integration, this yielded five models for comparative performance evaluation, with the results presented in Supplementary Figure S4(f). To ensure fairness, all these models employed the same network architecture, training hyperparameters, convergence criteria, and other training/testing conditions, differing only in the number of frames used to generate their input images.

Other implementation details

All the image preprocessing and dataset preparations were performed using MATLAB, version R2022b (MathWorks). The codes for training the swarming classification DNN models were developed in Python 3.7.11, utilizing PyTorch 1.10.1. All the network training and testing tasks were carried out on a desktop computer equipped with an Intel Core i9-10920X CPU, 256GB of memory, and an Nvidia GeForce RTX 3090 GPU.

Network evaluation

To evaluate the classification performance of our deep learning-based swarming classifier, we used the measurements of sensitivity and specificity, defined as

$$\text{sensitivity} = \frac{TP}{TP + FN} \quad (5)$$

$$\text{specificity} = \frac{TN}{TN + FP} \quad (6)$$

where *TP* means true positives, *TN* means true negatives, *FP* means false positives, and *FN* means false negatives.

Moreover, in the t-SNE analysis to highlight features of false positives and false negatives, the same inputs used for our deep learning-based classifier were processed by a pre-trained VGG-16 model⁵³ used for feature extraction. The extracted features were then reduced in dimensionality using the t-SNE method, and the resulting two-dimensional projections are presented in Supplementary Figure S5(b) using the default settings provided in the PyTorch library.

Acknowledgments

We thank Cornelia Bargman at Rockefeller University for gifting us the bacterial strains *Serratia marcescens* DB10. S. M. and Albert Einstein College of Medicine acknowledge a former grant received by Weijie Chen from the National Postdoc Foundation (KLF1340031), China.

Disclosure statement

Sridhar Mani and Hao Li filed a U.S. patent application (Application No. 15/765,513; PCT/US2016/052742 (and WO2017062175A1). A prior Provisional Patent Application # (63033369) was filed: Identifying Bacterial Motility via Micro Biochip Confinement; co-inventors: Weijie C, Mani N, Mani S, Tang J. Sridhar Mani is a scientific advisor to Symberix INC (NC, USA) and Lishan Biotechnology (Shanghai, CN).

Funding

The work was supported by the internal funds of UCLA and Albert Einstein College of Medicine.

ORCID

Aydogan Ozcan  <http://orcid.org/0000-0002-0717-683X>

Author Contributions

S.M. and A.O. conceived the research. H.L., N.M., and W. C. conducted all bacteria swarming/swimming experiments and imaged all videos used in this work. Y.L., K. O., Y.Q., N.M., and T.L. developed the image processing and network training/testing codes. Y.L. and K. O. processed the data and prepared the dataset. Y.L., Y.

Q., and K.O. trained the neural network. W.C., Y.L., H.L., and N.M. performed the result analysis. Y.L., W.C., N.M., H.L., S.M., and A.O. prepared the manuscript, and all authors contributed to the manuscript. S.M. and A. O. supervised the research. Y. Li, H. Li, and W. Chen contributed equally to this work.

Code availability

Deep learning models reported in this work used standard libraries and scripts that are publicly available in PyTorch. Trained models and the testing codes can be found at: https://github.com/liyuzhu1998/Swarming_Detection_ExampleImgs_Codes.

Data availability statement

The authors declare that all data supporting the results of this study are available within the main text and the Supplementary Information. Example testing images can be found at: https://github.com/liyuzhu1998/Swarming_Detection_ExampleImgs_Codes.

Significant statement

Our study addresses the critical challenge of differentiating bacterial swarming from swimming, two key forms of motility relevant to both bacterial pathogenesis and therapeutic potential. Traditionally, swarming detection has relied on manual, time-consuming methods that are susceptible to human bias. In contrast, we introduce, for the first time, a deep learning-based classifier that rapidly and accurately predicts swarming probability from a single blurry image with a long integration time, offering a quantitative and automated approach suited for high-throughput environments.

References

1. Webre DJ, Wolanin PM, Stock JB. Bacterial chemotaxis. *Curr Biol*. 2003;13(2):R47–R49. doi: 10.1016/S0960-9822(02)01424-0.
2. Kearns DB. A field guide to bacterial swarming motility. *Nat Rev Microbiol*. 2010;8(9):634–644. doi: 10.1038/nrmicro2405.
3. Klein RD, Hultgren SJ. Urinary tract infections: microbial pathogenesis, host–pathogen interactions and new treatment strategies. *Nat Rev Microbiol*. 2020;18(4):211–226. doi: 10.1038/s41579-020-0324-0.
4. Arikawa K, Nishikawa Y. Interleukin-8 induction due to diffusely adherent *Escherichia coli* possessing Afa/Dr genes depends on flagella and epithelial Toll-like receptor 5. *Microbiol And Immunol*. 2010;54(9):491–501. doi: 10.1111/j.1348-0421.2010.00244.x.

5. Mitra A, Palaniyandi S, Herren CD, Zhu X, Mukhopadhyay S, Driks A. Pleiotropic roles of uvrY on biofilm formation, motility and virulence in uropathogenic *Escherichia coli* CFT073. *PLOS ONE*. 2013;8(2):e55492. doi: [10.1371/journal.pone.0055492](https://doi.org/10.1371/journal.pone.0055492).
6. Lane MC, Alteri CJ, Smith SN, Mobley HLT. Expression of flagella is coincident with uropathogenic *Escherichia coli* ascension to the upper urinary tract. *Proc Natl Acad Sci USA*. 2007;104(42):16669–16674. doi: [10.1073/pnas.0607898104](https://doi.org/10.1073/pnas.0607898104).
7. Armbruster CE, Mobley HLT. Merging mythology and morphology: the multifaceted lifestyle of proteus mirabilis. *Nat Rev Microbiol*. 2012;10(11):743–754. doi: [10.1038/nrmicro2890](https://doi.org/10.1038/nrmicro2890).
8. Armbruster CE, Hodges SA, Mobley HLT. Initiation of swarming motility by proteus mirabilis occurs in response to specific cues present in urine and requires excess L-glutamine. *J Bacteriol*. 2013;195(6):1305–1319. doi: [10.1128/JB.02136-12](https://doi.org/10.1128/JB.02136-12).
9. Schaffer JN, Pearson MM, Mulvey MA, Stapleton AE, Klumpp DJ. Proteus mirabilis and urinary tract infections. *Microbiol Spectr*. 2015;3(5). doi: [10.1128/microbiolspec.UTI-0017-2013](https://doi.org/10.1128/microbiolspec.UTI-0017-2013).
10. Armbruster CE, Mobley HLT, Pearson MM, Donnenberg MS. Pathogenesis of proteus mirabilis infection. *EcoSal Plus*. 2018;8(1). doi: [10.1128/ecosalplus.esp-0009-2017](https://doi.org/10.1128/ecosalplus.esp-0009-2017).
11. De A, Chen W, Li H, Wright JR, Lamendella R, Lukin DJ, Szymczak WA, Sun K, Kelly L, Ghosh S, et al. Bacterial swimmers enriched during intestinal stress ameliorate damage. *Gastroenterology*. 2021;161(1):211–224. doi: [10.1053/j.gastro.2021.03.017](https://doi.org/10.1053/j.gastro.2021.03.017).
12. Elhenawy W, Tsai CN, Coombes BK. Host-specific adaptive diversification of Crohn's disease-associated adherent-invasive *Escherichia coli*. *Cell Host & Microbe*. 2019;25(2):301–312.e5. doi: [10.1016/j.chom.2018.12.010](https://doi.org/10.1016/j.chom.2018.12.010).
13. Chen W, Mani N, Karani H, Li H, Mani S, Tang JX. Confinement discerns swimmers from planktonic bacteria. *eLife*. 2021;10:e64176. doi: [10.7554/eLife.64176](https://doi.org/10.7554/eLife.64176).
14. Li Y, Zhai H, Sanchez S, Kearns DB, Wu Y. Noncontact cohesive swimming of bacteria in two-dimensional liquid films. *Phys Rev Lett*. 2017;119(1):018101. doi: [10.1103/PhysRevLett.119.018101](https://doi.org/10.1103/PhysRevLett.119.018101).
15. Beppu K, Izri Z, Gohya J, Eto K, Ichikawa M, Maeda YT. Geometry-driven collective ordering of bacterial vortices. *Soft Matter*. 2017;13(29):5038–5043. doi: [10.1039/C7SM00999B](https://doi.org/10.1039/C7SM00999B).
16. Patteson AE, Gopinath A, Arratia PE. The propagation of active-passive interfaces in bacterial swarms. *Nat Commun*. 2018;9(1):5373. doi: [10.1038/s41467-018-07781-y](https://doi.org/10.1038/s41467-018-07781-y).
17. Mamoshina P, Vieira A, Putin E, Zhavoronkov A. Applications of deep learning in biomedicine. *Mol Pharm*. 2016;13(5):1445–1454. doi: [10.1021/acs.molpharmaceut.5b00982](https://doi.org/10.1021/acs.molpharmaceut.5b00982).
18. Wang H, Ceylan Koydemir H, Qiu Y, Bai B, Zhang Y, Jin Y, Tok S, Yilmaz EC, Gumustekin E, Rivenson Y, et al. Early detection and classification of live bacteria using time-lapse coherent imaging and deep learning. *Light Sci Appl*. 2020;9(1):118. doi: [10.1038/s41377-020-00358-9](https://doi.org/10.1038/s41377-020-00358-9).
19. Göröcs Z, Baum D, Song F, de Haan K, Ceylan Koydemir H, Qiu Y, Cai Z, Skandakumar T, Peterman S, Tamamitsu M, et al. Label-free detection of giardia lamblia cysts using a deep learning-enabled portable imaging flow cytometer. *Lab Chip*. 2020;20(23):4404–4412. doi: [10.1039/D0LC00708K](https://doi.org/10.1039/D0LC00708K).
20. Liang C-M, Lai C-C, Wang S-H, Lin Y-H. Environmental microorganism classification using optimized deep learning model. *Environ Sci Pollut Res*. 2021;28(24):31920–31932. doi: [10.1007/s11356-021-13010-9](https://doi.org/10.1007/s11356-021-13010-9).
21. Li Y, Liu T, Koydemir HC, Wang H, O'Riordan K, Bai B, Haga Y, Kobashi J, Tanaka H, Tamaru T, et al. Deep learning-enabled detection and classification of bacterial colonies using a thin-film transistor (TFT) image sensor. *ACS Photonics*. 2022;9(7):2455–2466. doi: [10.1021/acsp Photonics.2c00572](https://doi.org/10.1021/acsp Photonics.2c00572).
22. Liu T, Li Y, Koydemir HC, Zhang Y, Yang E, Eryilmaz M, Wang H, Li J, Bai B, Ma G, et al. Rapid and stain-free quantification of viral plaque via lens-free holography and deep learning. *Nat Biomed Eng*. 2023;7(8):1040–1052. doi: [10.1038/s41551-023-01057-7](https://doi.org/10.1038/s41551-023-01057-7).
23. Ma P, Li C, Rahaman MM, Yao Y, Zhang J, Zou S, Zhao X, Grzegorzec M. A state-of-the-art survey of object detection techniques in microorganism image analysis: from classical methods to deep learning approaches. *Artif Intell Rev*. 2023;56(2):1627–1698. doi: [10.1007/s10462-022-10209-1](https://doi.org/10.1007/s10462-022-10209-1).
24. Pandya MD, Shah PD, Jardosh S. Chapter 3 - medical image diagnosis for disease detection: a deep learning approach. In: Dey, N., Ashour, A. S., Fong, S. J. Borra, editors. *U-Healthcare monitoring systems*. Academic Press; 2019. p. S.) 37–60. doi: [10.1016/B978-0-12-815370-3.00003-7](https://doi.org/10.1016/B978-0-12-815370-3.00003-7).
25. Joung H-A, Ballard ZS, Wu J, Tseng DK, Teshome H, Zhang L, Horn EJ, Arnaboldi PM, Dattwyler RJ, Garner OB, et al. Point-of-care serodiagnostic test for early-stage lyme disease using a multiplexed paper-based immunoassay and machine learning. *ACS Nano*. 2020;14(1):229–240. doi: [10.1021/acsnano.9b08151](https://doi.org/10.1021/acsnano.9b08151).
26. Kumaraswamy E, Sharma S, Kumar S. A review on cancer detection strategies with help of biomedical images using machine learning techniques. *AIP Conference Proceedings*; Vol. 2418. 2022. p. 030064.
27. Jiang X, Hu Z, Wang S, Zhang Y. Deep learning for medical image-based cancer diagnosis. *Cancers (Basel)*. 2023;15(14):3608. doi: [10.3390/cancers15143608](https://doi.org/10.3390/cancers15143608).
28. Ghosh R, Joung H-A, Goncharov A, Palanisamy B, Ngo K, Pejcinovic K, Krockenberger N, Horn EJ,

- Garner OB, Ghazal E, et al. Rapid single-tier serodiagnosis of lyme disease. *Nat Commun.* **2024**;15(1):7124. doi: [10.1038/s41467-024-51067-5](https://doi.org/10.1038/s41467-024-51067-5).
29. Tobore I, Li J, Yuhang L, Al-Handarish Y, Kandwal A, Nie Z, Wang L. Deep learning intervention for health care challenges: some biomedical domain considerations. *JMIR Mhealth Uhealth.* **2019**;7(8): e11966. doi: [10.2196/11966](https://doi.org/10.2196/11966).
 30. Shrestha P, Kuang N, Yu J. Efficient end-to-end learning for cell segmentation with machine generated weak annotations. *Commun Biol.* **2023**;6(1):1–10. doi: [10.1038/s42003-023-04608-5](https://doi.org/10.1038/s42003-023-04608-5).
 31. Nešić N, Heiligenstein X, Zopf L, Blüml V, Keuenhof KS, Wagner M, Höög JL, Qi H, Li Z, Tsaramirsis G, et al. Automated segmentation of cell organelles in volume electron microscopy using deep learning. *Microsc Res Tech.* **2024**;87(8):1718–1732. doi: [10.1002/jemt.24548](https://doi.org/10.1002/jemt.24548).
 32. Schoppe O, Pan C, Coronel J, Mai H, Rong Z, Todorov MI, Müskes A, Navarro F, Li H, Ertürk A, et al. Deep learning-enabled multi-organ segmentation in whole-body mouse scans. *Nat Commun.* **2020**;11(1):5626. doi: [10.1038/s41467-020-19449-7](https://doi.org/10.1038/s41467-020-19449-7).
 33. Ma Y. Classification of bacterial motility using machine learning. Masters Theses. **2020**.
 34. Riekeles M, Schirmack J, Schulze-Makuch D. Machine learning algorithms applied to identify microbial species by their motility. *Life.* **2021**;11(1):44. doi: [10.3390/life11010044](https://doi.org/10.3390/life11010044).
 35. Mayer B, Holtrup S, Graumann PL. A machine learning-empowered workflow to discriminate *Bacillus subtilis* motility phenotypes. *BioMedinformatics.* **2022**;2(4):565–579. doi: [10.3390/biomedinformatics2040036](https://doi.org/10.3390/biomedinformatics2040036).
 36. Jeckel H, Jelli E, Hartmann R, Singh P, Mok R, Totz J, Vidakovic L, Eckhardt B, Dunkel J, Drescher K, et al. Learning the space-time phase diagram of bacterial swarm expansion. *Proceedings of the National Academy of Sciences*; Vol. **116**. **2019**. p. 1489–1494.
 37. Huang G, Liu Z, Pleiss G, Maaten LVD, Weinberger KQ. Convolutional networks with dense connectivity. *Ieee T Pattern Anal.* **2022**;44(12):8704–8716. doi: [10.1109/TPAMI.2019.2918284](https://doi.org/10.1109/TPAMI.2019.2918284).
 38. Köves B, Salvador E, Grönberg-Hernández J, Zdziarski J, Wullt B, Svanborg C, Dobrindt U. Rare emergence of symptoms during long-Term asymptomatic *Escherichia coli* 83972 carriage without an altered virulence factor repertoire. *J Urol.* **2014**;191(2):519–528. doi: [10.1016/j.juro.2013.07.060](https://doi.org/10.1016/j.juro.2013.07.060).
 39. Wang W, Huang X, Yang H, Niu X, Li D, Yang C, Li L, Zou L, Qiu Z, Wu S, et al. Antibacterial activity and Anti-quorum sensing mediated phenotype in response to essential oil from *Melaleuca bracteata* leaves. *Int J Mol Sci.* **2019**;20(22):5696. doi: [10.3390/ijms20225696](https://doi.org/10.3390/ijms20225696).
 40. Abbas HA, Hegazy WAH, Blumenthal RM. Repurposing anti-diabetic drug “sitagliptin” as a novel virulence attenuating agent in *Serratia marcescens*. *PLOS ONE.* **2020**;15(4):e0231625. doi: [10.1371/journal.pone.0231625](https://doi.org/10.1371/journal.pone.0231625).
 41. Abbas HA, Shaldam MA, Eldamasi D. Curtailing Quorum Sensing in *Pseudomonas aeruginosa* by Sitagliptin. *Curr Microbiol.* **2020**;77(6):1051–1060. doi: [10.1007/s00284-020-01909-4](https://doi.org/10.1007/s00284-020-01909-4).
 42. Lawrence JA, Huang Z, Rathinavelu S, Hu J-F, Garo E, Ellis M, Norman VL, Buckle R, Williams RB, Starks CM, et al. Optimized plant compound with potent anti-biofilm activity across gram-negative species. *Bioorg Med Chem.* **2020**;28(5):115229. doi: [10.1016/j.bmc.2019.115229](https://doi.org/10.1016/j.bmc.2019.115229).
 43. Li C, Jiang C, Jing H, Jiang C, Wang H, Du X, Lou Z. Separation of phenolics from peony flowers and their inhibitory activities and action mechanism on bacterial biofilm. *Appl Microbiol Biotechnol.* **2020**;104(10):4321–4332. doi: [10.1007/s00253-020-10540-z](https://doi.org/10.1007/s00253-020-10540-z).
 44. Li T, Sun X, Chen H, He B, Mei Y, Wang D, Li J. Methyl anthranilate: a novel quorum sensing inhibitor and anti-biofilm agent against *aeromonas sobria*. *Food Microbiol.* **2020**;86:103356. doi: [10.1016/j.fm.2019.103356](https://doi.org/10.1016/j.fm.2019.103356).
 45. Parasuraman P, Devadatha B, Sarma VV, Ranganathan S, Ampasala DR, Siddhardha B. Anti-quorum sensing and antibiofilm activities of *Blastobotrys parvus* PPR3 against *Pseudomonas aeruginosa* PAO1. *Microb Pathog.* **2020**;138:103811. doi: [10.1016/j.micpath.2019.103811](https://doi.org/10.1016/j.micpath.2019.103811).
 46. Proctor CR, McCarron PA, Ternan NG. Furanone quorum-sensing inhibitors with potential as novel therapeutics against *Pseudomonas aeruginosa*. *J Med Microbiol.* **2020**;69(2):195–206. doi: [10.1099/jmm.0.001144](https://doi.org/10.1099/jmm.0.001144).
 47. Rütshlin S, Böttcher T. Inhibitors of bacterial swarming behavior. *Chem A Eur J.* **2020**;26(5):964–979. doi: [10.1002/chem.201901961](https://doi.org/10.1002/chem.201901961).
 48. Dobrijevic D, Abraham A-L, Jamet A, Maguin E, Guchte MVD, Cappello F. Functional comparison of bacteria from the human Gut and closely related non-Gut bacteria reveals the importance of conjugation and a paucity of motility and chemotaxis functions in the Gut environment. *PLOS ONE.* **2016**;11(7): e0159030. doi: [10.1371/journal.pone.0159030](https://doi.org/10.1371/journal.pone.0159030).
 49. Li H, Hong L, Szymczak W, Orner E, Garber AI, Cooper VS, Chen W, De A, Tang JX, Mani S, et al. Protocol for isolating single species of bacteria with swarming ability from human feces. *STAR Protoc.* **2024**;5(2):102961. doi: [10.1016/j.xpro.2024.102961](https://doi.org/10.1016/j.xpro.2024.102961).
 50. Nagao-Kitamoto H, Shreiner AB, Gilliland MG, Kitamoto S, Ishii C, Hirayama A, Kuffa P, El-Zaatari M, Grasberger H, Seekatz AM, et al. Functional characterization of inflammatory bowel disease-associated gut dysbiosis in gnotobiotic mice. *Cellular Mol Gastroenterol Hepatol.* **2016**;2(4):468–481. doi: [10.1016/j.jcmgh.2016.02.003](https://doi.org/10.1016/j.jcmgh.2016.02.003).
 51. Araujo G, Chen W, Mani S, Tang JX. Orbiting of flagellated bacteria within a thin fluid film around

- micrometer-sized particles. *Biophys J.* **2019**;117(2):346–354. doi: [10.1016/j.bpj.2019.06.005](https://doi.org/10.1016/j.bpj.2019.06.005).
52. Maaten LVD, Hinton G. Visualizing Data using t-SNE. *J Mach Learn Res.* **2008**;9:2579–2605.
 53. Simonyan K, Zisserman A. Very deep convolutional networks for large-scale image recognition. Preprint at **2015**; doi: [10.48550/arXiv.1409.1556](https://doi.org/10.48550/arXiv.1409.1556).
 54. Abdulkadieva MM, Sysolyatina EV, Vasilieva EV, Gusarov AI, Domnin PA, Slonova DA, Stanishevskiy YM, Vasiliev MM, Petrov OF, Ermolaeva SA, et al. Strain specific motility patterns and surface adhesion of virulent and probiotic *Escherichia coli*. *Sci Rep.* **2022**;12(1):614. doi: [10.1038/s41598-021-04592-y](https://doi.org/10.1038/s41598-021-04592-y).
 55. Schuerle S, Soleimany AP, Yeh T, Anand GM, Häberli M, Fleming HE, Mirkhani N, Qiu F, Hauert S, Wang X, et al. Synthetic and living micropellers for convection-enhanced nanoparticle transport. *Sci Adv.* **2019**;5(4):eaav4803. doi: [10.1126/sciadv.aav4803](https://doi.org/10.1126/sciadv.aav4803).
 56. Kim JA, Hou Y, Keshavarz M, Yeatman EM, Thompson AJ. Characterization of bacteria swarming effect under plasmonic optical fiber illumination. *J Biomed Opt.* **2023**;28(7):075003. doi: [10.1117/1.JBO.28.7.075003](https://doi.org/10.1117/1.JBO.28.7.075003).
 57. Raina J-B, Fernandez V, Lambert B, Stocker R, Seymour JR. The role of microbial motility and chemotaxis in symbiosis. *Nat Rev Microbiol.* **2019**;17(5):284–294. doi: [10.1038/s41579-019-0182-9](https://doi.org/10.1038/s41579-019-0182-9).
 58. Shao J, Liu Y, Xie J, Štefanič P, Lv Y, Fan B, Mandic-Mulec I, Zhang R, Shen Q, Xu Z, et al. Annulment of bacterial antagonism improves plant beneficial activity of a *Bacillus velezensis* consortium. *Appl Environ Microb.* **2022**;88(8). doi: [10.1128/aem.00240-22](https://doi.org/10.1128/aem.00240-22).
 59. Alagely A, Krediet CJ, Ritchie KB, Teplitski M. Signaling-mediated cross-talk modulates swarming and biofilm formation in a coral pathogen *Serratia marcescens*. *The ISME J.* **2011**;5(10):1609–1620. doi: [10.1038/ismej.2011.45](https://doi.org/10.1038/ismej.2011.45).
 60. Tout J, Jeffries TC, Petrou K, Tyson GW, Webster NS, Garren M, Stocker R, Ralph PJ, Seymour JR. Chemotaxis by natural populations of coral reef bacteria. *The ISME J.* **2015**;9(8):1764–1777. doi: [10.1038/ismej.2014.261](https://doi.org/10.1038/ismej.2014.261).
 61. Garren M, Son K, Tout J, Seymour JR, Stocker R. Temperature-induced behavioral switches in a bacterial coral pathogen. *The ISME J.* **2016**;10(6):1363–1372. doi: [10.1038/ismej.2015.216](https://doi.org/10.1038/ismej.2015.216).
 62. Gao C, Garren M, Penn K, Fernandez VI, Seymour JR, Thompson JR, Raina J-B, Stocker R. Coral mucus rapidly induces chemokinesis and genome-wide transcriptional shifts toward early pathogenesis in a bacterial coral pathogen. *The ISME J.* **2021**;15(12):3668–3682. doi: [10.1038/s41396-021-01024-7](https://doi.org/10.1038/s41396-021-01024-7).
 63. Byju AS, Patel D, Chen W, Mani S. Assessing swarming of aerobic bacteria from human fecal matter. *Bio Protoc.* **2021**;11(9):e4008. doi: [10.21769/BioProtoc.4008](https://doi.org/10.21769/BioProtoc.4008).
 64. Pozo F, Borbor M, Solórzano R, Sonnenholzner S, Bayot B. Optimized swarming motility assay to identify anti-virulence products against *Vibrio parahaemolyticus*, a pathogen of farmed shrimp. *MethodsX.* **2024**;12:102622. doi: [10.1016/j.mex.2024.102622](https://doi.org/10.1016/j.mex.2024.102622).
 65. Depardieu F, Bikard D. Gene silencing with CRISPRi in bacteria and optimization of dCas9 expression levels. *Methods.* **2020**;172:61–75. doi: [10.1016/j.ymeth.2019.07.024](https://doi.org/10.1016/j.ymeth.2019.07.024).
 66. Kingma DP, Ba J. Adam: a method for stochastic optimization. *arXiv org.* **2014**; doi: <https://arxiv.org/abs/1412.6980v9>.